

WR 140 in the Infrared

Peredur Williams

Institute for Astronomy, Royal Observatory, Edinburgh, UK

Published in proceedings of

”Stellar Winds in Interaction”, editors T. Eversberg and J.H. Knapen.

Full proceedings volume is available on <http://www.stsci.de/pdf/arrabida.pdf>

Abstract: Observations in the infrared have played a significant rôle in the development of our understanding of WR 140. Two sets of observations are described here: the changing profile of the 1.083- μm He I line observed for the 2009 campaign to study evolution of the wind-collision region near periastron passage, and multi-wavelength photometry and imaging of the dust made by WR 140 in previous periastron passages.

1 Introduction

In his contribution, Tony Moffat has described the properties of WR 140 (= HD 193793) and the motivation for the 2009 campaign. Fundamental to colliding-wind binaries is the power in their winds. The WC7 and O5 stars in WR 140 have fast ($\sim 3000 \text{ km}^{-1}$) winds carrying $\sim 2 \times 10^{-5}$ and $\sim 2 \times 10^{-6} M_{\odot} \text{ y}^{-1}$ mass-loss respectively. The kinetic powers of these winds are in excess of 10^4 and $10^3 L_{\odot}$. Of these, $\sim 3 \times 10^3 L_{\odot}$ is dissipated where the winds collide (the wind-collision region, WCR), leading to shock-heating and compression of the plasma, X ray emission, synchrotron radio emission, changes to the profiles of some emission lines and condensation of ‘dust’ (really something like soot) in the shock-compressed wind. Of these effects, dust formation was certainly the most unexpected. The 1977 dust formation episode from WR 140 was independently discovered (Williams et al. 1977, 1978) at the 1.5-m Infrared Flux Collector (now the Carlos Sánchez Telescope) at Izaña on Tenerife – only a short distance from the Mons telescope.

From 1977 to the 2001 periastron, the thermal emission from dust made by WR 140 was tracked with infrared photometers at a variety of wavelengths between 1 and 20 μm and, in the years following the 2001 dust-formation episode, with infrared cameras which imaged the dust clouds. These observations have been published, but I will summarise the most recent work (Williams et al. 2009) to show how much we can learn from observing in this wavelength domain.

For the 2009 campaign, we (Watson Varricatt, Andy Adamson and the author) extended the observations of the 1.083- μm He I line taken around the 2001 periastron passage (Varicatt, Williams & Ashok 2004). This line has a P Cygni profile, with a flat-topped emission component like the $\lambda 5696 \text{ \AA}$ C III line observed in the optical campaign, and develops a strong sub-peak near periastron passage. Its absorption component varies as we observe the stars through different parts of the wind. The new

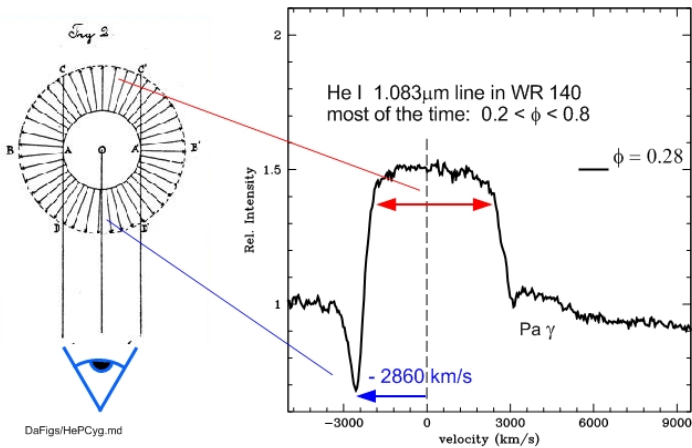


Figure 1: P-Cygni profile of the He I 1.083- μm line for *most* of the orbit. The weak emission feature marked Pa γ more probably comes from the hydrogenic He II and C IV transitions at this wavelength.

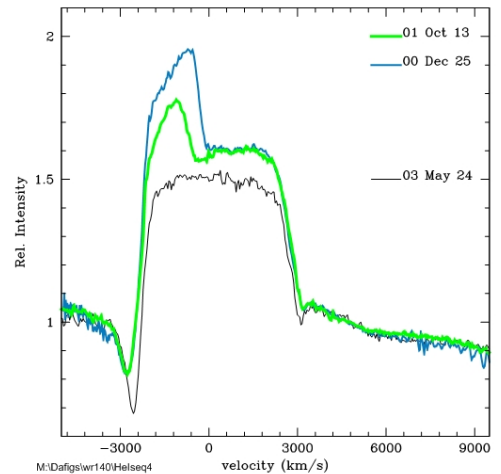


Figure 2: Profiles of the 1.083- μm line showing development of the sub-peak at phases 0.96 and 0.986.

observations were taken in 2008 with UIST on the United Kingdom Infrared Telescope (UKIRT) at a resolution of 200 km s^{-1} and comprise five spectra extending the coverage to earlier phases ($\phi = 0.93\text{--}0.95$) and nine spectra near $\phi = 0.99$, when the WR 140 system was changing very rapidly.

2 Geometry of the WCR from the 1.083- μm He I line profile

Spectra of WR 140 in the region of the 1.083- μm He I line are shown in Figs 1¹ and 2. The first spectra of this line in WR 140 were taken in a programme to measure stellar wind terminal velocities, v_∞ , and not near periastron. The profiles in Fig. 2 come from the study by Varricatt et al., and show rapid development of the sub-peak as WR 140 approached the 2001 periastron.

The WCR (Fig. 3) lies where the dynamic pressures of the WC7 and O5 stellar winds balance. Its shape can be calculated (e.g. Cantó, Raga & Wilkin 1996) from the ratio of the momenta of the two stellar winds, $\eta = (\dot{M}v_\infty)_{\text{O5}}/(\dot{M}v_\infty)_{\text{WC7}}$, and is closer to the O5 star because its mass-loss rate and wind momentum are much lower than that of the WC star. At large distances from the stars, the WCR can be approximated by a cone (opening angle θ), which is twisted to form a spiral in the orbital plane by the orbital motion. The pitch angle of the spiral depends on the ratio of the transverse velocity of the stars in their orbit relative to stellar wind velocities. In an elliptical orbit like that of WR 140, this ratio varies significantly (factor > 15), so the breadth of the spiral varies hugely round the orbit – a bit like a snake which has swallowed a large animal.

The WC7 and O5 stellar winds are shocked on each side of the WCR in regions which are wide if the shocks are adiabatic (most of the time in the case of WR 140) but very thin if the shocks are radiative (only around periastron). These shocks compress the winds, which flow along the WCR (only that of the WC7 star is shown in the figure). The compressed wind accelerates from the stagnation point to an asymptotic value, V_{flow} , on the ‘conical’ region of the WCR, and can be calculated from the stellar winds following Cantó et al. It is in the compressed WC7 stellar wind, comprising mostly helium and carbon ions, that we believe the He I and C III sub-peak emission features form.

¹The sketch of an expanding stellar envelope showing where the absorption and emission components are formed dates from the first published interpretation of such a profile, in a nova spectrum in 1804, by Jakob Halm, of the Royal Observatory Edinburgh.

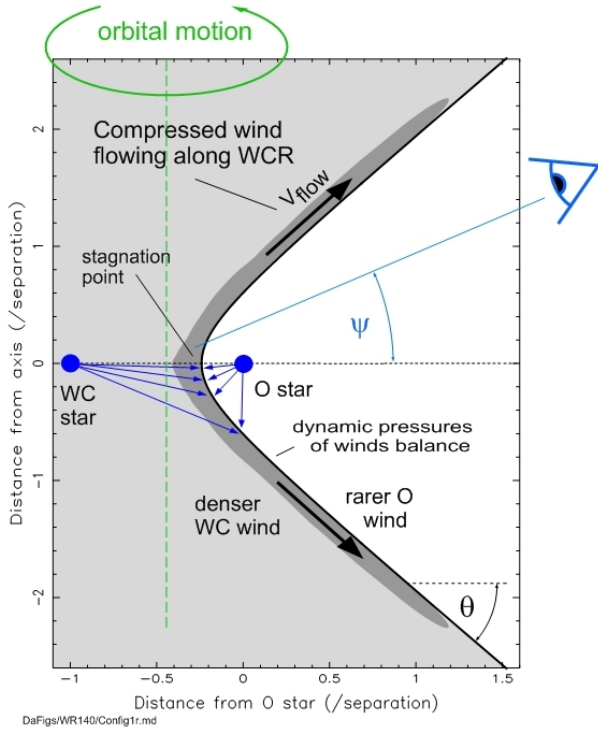


Figure 3: A slice through the WCR perpendicular to the orbital plane. The stars and WCR rotate about the vertical axis.

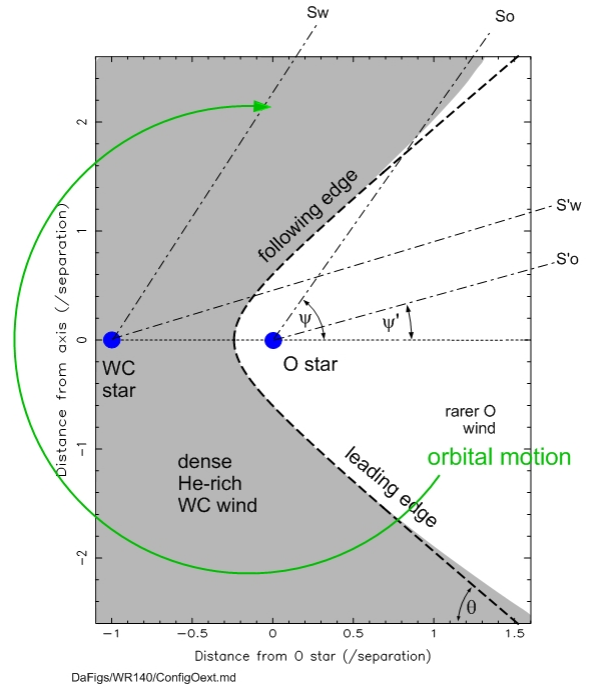


Figure 4: A view of the WCR in the plane including the observer, showing how the lines of sight to the stars vary with orbital phase.

What we observe in the line profile, in terms of sub-peak emission and absorption of the underlying stars, depends on our line of sight, which makes an angle ψ with the axis (WC7–O5) joining the stars. This viewing angle ψ varies round the orbit as $\cos \psi = -\sin i \sin(f + \omega)$, where ω is determined from the RV orbit, the inclination, i , comes from other observations, e.g. an astrometric orbit, and f is the true anomaly, the P.A. of the stars in their orbit. Owing to the high eccentricity of the orbit, the variation of f with phase is very sensitive to the elements of the RV orbit. Work for this contribution used those of Marchenko et al. (2003), and some of the results may be different when they are re-calculated using the definitive orbit from the 2009 campaign.

The strength of the $1.083\text{-}\mu\text{m}$ absorption varies significantly (Figs 2 and 5). The underlying continuum comes from both the WC7 and O5 stars. In Fig. 4 we see the WCR from a different viewpoint: above the plane including the observer, to show how our sightlines $S'o$ and S_o to the O5 star and $S'w$ and S_w to the WC7 star change with the orbital motion. The WCR is asymmetric: as we move away from the stars, it lags behind the WC–O axis and cone because of the orbital motion, eventually to form the variable-width spiral. The stars and WCR move clockwise in this figure, so progressively later sightlines to the observer occur in the opposite sense. We see that the WC7 star is always viewed through some of its own wind, nearest the star. As this star is also the fainter component in the one-micron region, most of the variation observed in the $1.083\text{-}\mu\text{m}$ line absorption component must come from the variation in absorption to the O5 star. When the viewing angle is small, near conjunction (ψ' in Fig. 4), the O5 star is seen through its own wind (sightline $S'o$), which has one-tenth the density of the WC7 wind and a significantly lower helium abundance, so the absorption is at its lowest. This can be seen in Fig 5, where the absorption is least near conjunction (O5 star in front) and barely changes when we observe it through the O5 stellar wind alone between the first observation and $\phi = 0.985$, when it suddenly rises sharply. This must be the phase at which the following edge of the WCR crosses our sightline to the O5 star (Figs 4 and 6, i.e. when the viewing

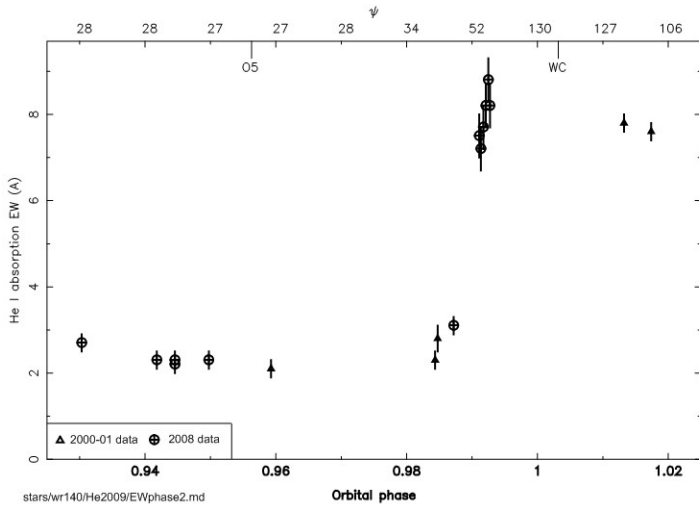


Figure 5: EW of absorption component as a function of phase near periastron. On top are the viewing angle, ψ , and phases of conjunction, ‘O5’ and ‘WC’, in front.

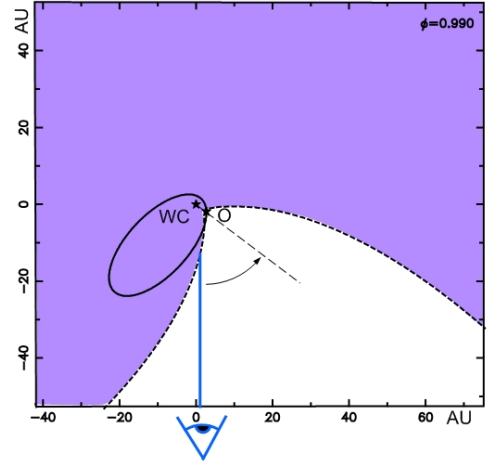


Figure 6: Sketch of the system at lower scale than Fig 4 for beginning of eclipse at $\phi = 0.990$.

angle, $\psi \simeq \theta$, the cone angle, and we begin to observe the O5 star through the more opaque WC7 stellar wind. Modelling the sharp increase of absorption (‘eclipse’) must account for the twisting of the WCR from the orbital motion, but we have a robust measure of the opening angle, $\theta = 50^\circ$ using the Marchenko et al. RV orbit and i from Dougherty et al. (2005). This implies a wind-momentum ratio $\eta = 0.10$ and a comparable mass-loss ratio, given the similarity of the wind velocities.

Spectra from the 2009 campaign showing the subpeak evolution are shown in Figs 7 and 8. The first spectrum shows a blue-shifted symmetric profile, which barely changed as the system moved through conjunction (July and August spectra, not shown here). In December, the profile had shifted, broadened and become asymmetrical. Modelling these changes requires knowledge of the geometry of the WCR, to be derived from the stellar winds, the orbit and the changes in the absorption component, the bulk velocity of the compressed flow (e.g. calculated following Cantó et al.) with the addition of an appropriate amount of turbulence, and then the line emissivity within the WCR, hopefully from the ever more sophisticated colliding wind models being calculated.

For a first pass, we can use the simplified geometry introduced by Lührs (1997), which considers only the conical region of the WCR, defined by θ , where the compressed flow velocity has reached its asymptotic value, V_{flow} . This requires only two parameters, which can be constant round the orbit, and has the further advantage that there is no need to know the location of the line emission or its spatial variation in the WCR. The down-wind spiral shape is modelled with a single tilt angle applied to the whole structure. This model has been successfully applied to model the sub-peaks in several system, mostly having almost circular orbits. The observed radial velocities of the sub-peak centre, RV_c , and extent, $\pm RV_{ext}$, can be related to the orbit via the viewing angle, ψ : $RV_c = V_{flow} \cos(\theta) \cos(\psi)$ and $RV_{ext} = V_{flow} \sin(\theta) \sin(\psi)$.

We apply this to WR 140 using our value of θ from the absorption profile and V_{flow} calculated following Cantó et al. and show the variation of RV_c , $RV_c + RV_{ext}$ and $RV_c - RV_{ext}$ with phase together with RV_c and extents (vertical bars) from our observed profiles in Fig 9. The RV_c curve reproduces the observed central velocities reasonably well but overestimates the RV extents before periastron and underestimates them afterwards. But when we come to calculate a line profile using the same model for the WCR, the fit (Fig. 10) is poor. Tuning parameters does not improve the fit, nor is twisting of the WCR for orbital motion likely to help: at $\phi = 0.94$, the transverse velocity is less than 2% of the wind velocities, and even less at earlier phases, which define the spiral at the time of

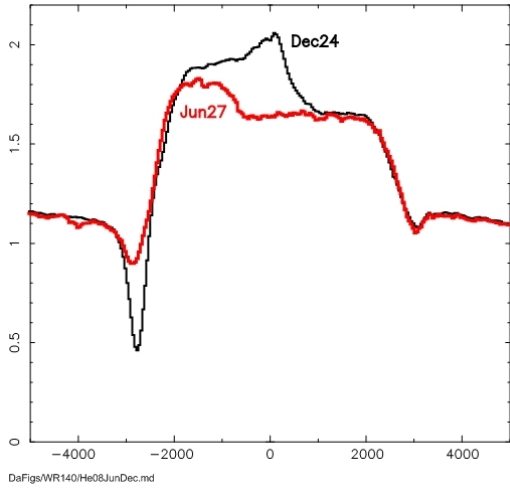


Figure 7: Spectra observed on 2008 Jun 27 and Dec 24 showing change of sub-peak profile as well as its movement to more positive velocity.

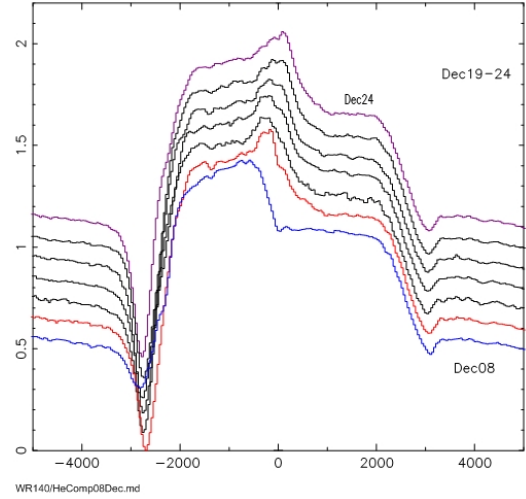


Figure 8: Montage of spectra showing evolution of sub-peak profile in 2008 December.

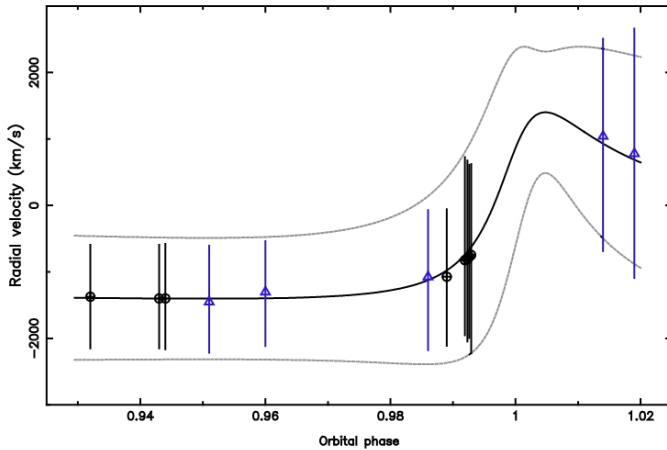


Figure 9: Measured central velocities (\oplus , \triangle) and extents (vertical bars) of He I sub-peaks compared with RV_c and $RV_c \pm RV_{ext}$ from a Lührs model.

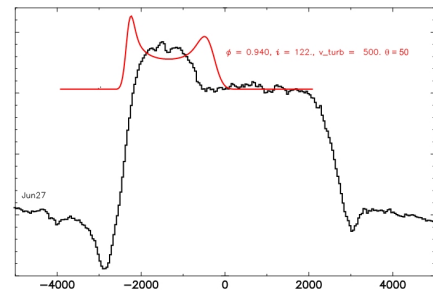


Figure 10: Model profile for sub-peak profile formed in a thin shell with same parameters. Apart from the central velocity, totally different.

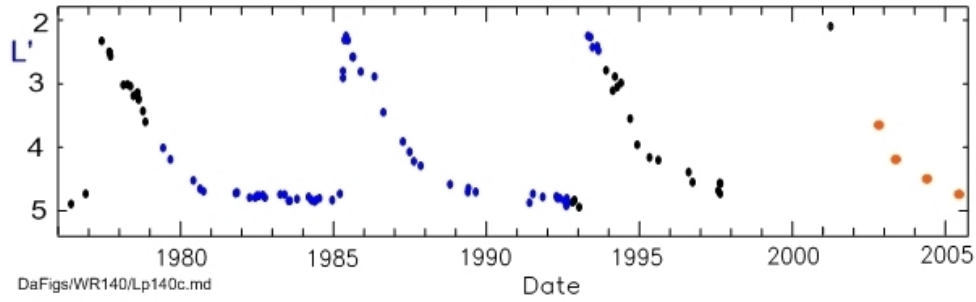


Figure 11: Light curve of WR 140 at $3.8\mu\text{m}$; data points in orange are from IR images; others from photometers on UKIRT (blue) or the IRFC/TCS, SPM, TIRGO, Calgary telescopes or published data (black).

observation².

Models including sub-peak line formation from the curved portion of the WCR, where wind is still accelerating, are more promising but require knowledge of the line emissivity with distance from the stagnation point, which requires detailed modelling of conditions in the WCR.

Returning to the observational data, it will be most interesting to compare the profiles of the $1.083\text{-}\mu\text{m}$ He I subpeaks with those observed on the 5696\AA C III line. Do the lines have similar profiles and central velocities? Is the variation of their intensity with, say, stellar separation the same? This will tell us whether they are formed in the same region of the WCR. These profiles and line shifts should also be compared with those the X-ray lines observed at high resolution (e.g. Pollock et al. 2005 and the present campaign) to build a self-consistent model of the WCR.

3 Infrared emission from dust made by WR 140

A dust grain located near a hot star with a strong stellar wind like WR 140 experiences three effects: heating by the stellar radiation, accelerative force from the stellar radiation and collision from ions in the stellar wind. The heated grain re-radiates at long wavelengths with a spectrum determined from the Planck function for its temperature and the grain emissivity law. There have been many laboratory experiments to make analogues of astronomical grains and measure their optical properties, and the best fits to WR star dust spectra come from amorphous carbon grains. Their emissivity laws have approximately the same wavelength dependence in the infrared, $\kappa \propto \lambda^{-1.1}$, so the grain temperature can be determined observationally. The spectrum of even a relatively small amount ($10^{-9}M_{\odot}$) of dust can readily be distinguished from that of a hot stellar wind using infrared observations at a few wavelengths between 1 and $10\mu\text{m}$, and the grain temperature and, less certainly, total mass of dust measured. From the grain's temperature, we can determine its distance from the star by considering the balance between its radiative heating and re-radiation because the heating depends on the geometric dilution of the stellar radiation field at the grain's distance. The equilibrium temperature T_g of a grain of radius a located at a distance r from a star of temperature T_* and radius R_* is related to these quantities through their Planck mean absorption cross-sections $\bar{Q}(a, T)$ appropriate to the grain or stellar temperature:

$$4\pi a^2 \bar{Q}(a, T_g) T_g^4 = \pi a^2 \bar{Q}(a, T_*) \frac{4\pi R_*^2 T_*^4}{4\pi r^2}$$

²Because the shape of the WCR in the orbital plane depends on the ratio of transverse to wind flow velocities at preceding phases, the shapes of the WCR at a particular phase interval before and after periastron will *not* be the same.

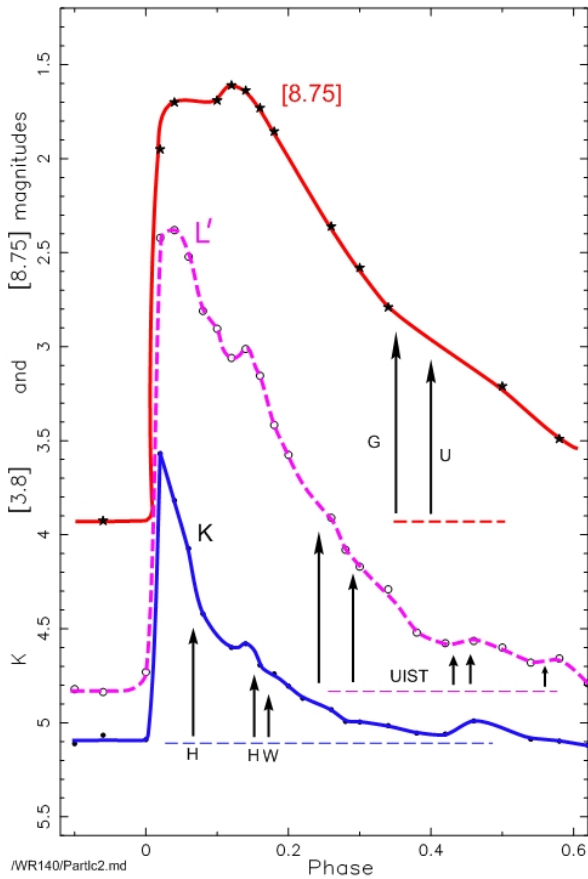


Figure 12: Light curves at $8.75\mu\text{m}$, $3.8\mu\text{m}$ (L') and $2.2\mu\text{m}$ (K) near maximum, showing also phases of imaging observations (see text).

For small amorphous carbon grains relevant to WR dust, $\overline{Q}(a, T) \propto aT$, and we get a handy relation between the equilibrium temperature of a grain and its distance from a star: $T_g \propto r^{-2/5}$. If the grain is too close to the star, its equilibrium temperature would be too high and it will evaporate; the corresponding distance is the closest at which grains can survive and is sometimes considered to be that at which they condense, the ‘nucleation radius’. A grain moving away from a star with the stellar wind, say, will inevitably cool and its infrared emission will fade. It follows that if we observe constant infrared emission from a WR star, as is sometimes the case, the dust being taken away in the wind must be being replenished by the formation of new grains at the same rate.

In the case of WR 140, the L' light curve (Fig 11) shows repeated episodes of dust formation ($\Delta L' = 2.5$), followed by fading of the emission as the grains move away from the stars. The wavelength of this curve ($3.8\mu\text{m}$) is optimal for studying WR dust formation because emission by newly formed dust peaks in this region while the flux from the stellar photosphere and wind have fallen off sufficiently by this wavelength for the dust emission to be conspicuous. This light curve and those in H and K , give periods of 2905 ± 10 d., 2905 ± 8 d. and 2900 ± 10 d. respectively, consistent with the RV orbit (2899 ± 1.3 d.).

As the fading of the IR emission is caused by cooling of the dust as it moves away from the stars, we expect light curves at shorter wavelengths to have steeper declines than those at long wavelengths, and this is largely observed (Fig. 12), where we see the fading in K is steeper than that in L' while that at $8.75\mu\text{m}$ is less steep. But if this was the whole story, the light curves at all wavelengths would start fading at the same time, while the observations show that the flux maxima occur later at longer

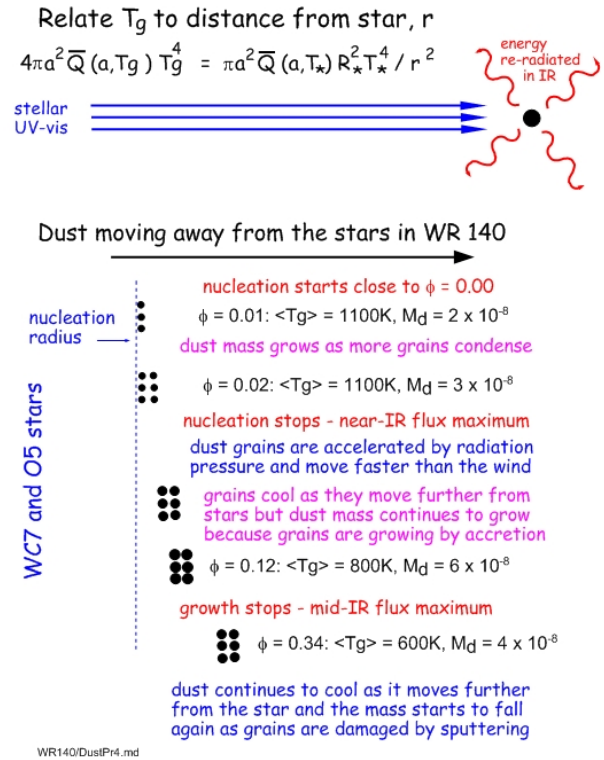


Figure 13: Cartoon of processes affecting the dust grains in the wind of WR 140

wavelengths; the 12.5- μm and 19.5- μm light curves resemble the 8.75- μm curve, and are even less steep.

From the multi-wavelength data, we can form spectral energy distributions (SEDs) for particular phases and model them to determine grain temperature and dust mass. The photometry tracks the integrated dust emission, so the temperature is an average, $\langle T_g \rangle$, of those of grains at different distances from the stars. Fits to the 1.6- to 19.5- μm and 1.6- to 12.5- μm data at phases 0.01 and 0.02 gave $\langle T_g \rangle \simeq 1100\text{K}$ and dust masses $M_d = 2 \times 10^{-8}$ and $3 \times 10^{-8} M_\odot$ respectively. The approximate constancy of $\langle T_g \rangle$, and therefore radiative-equilibrium distance from the stars, r , at these phases while the dust mass increased can be interpreted as continued condensation of new dust grains at a fixed distance from the stars, the ‘nucleation radius’. At $\phi = 0.00$, we have only *JHKL'* data and the fit to them gives $M_d \simeq 2 \times 10^{-10} M_\odot$, so it is evident that dust formation had just begun at periastron. By $\phi = 0.03$, the *JHKL'* magnitudes were fading and $\langle T_g \rangle$ was falling, indicating that no new dust was condensing to replenish the dust carried away with the wind. From $\phi = 0.03$ to $\phi = 0.12$, the near-IR flux fell while the mid-IR flux rose to maximum (Fig. 12). The model fits to the SEDs show that the dust mass doubled to $6 \times 10^{-8} M_\odot$ while $\langle T_g \rangle$ fell to 800 K at $\phi = 0.12$. This shows that the increase of dust mass was caused by the growth of the recently formed grains at their radiative equilibrium temperature rather than by the condensation of fresh grains at $T_g \simeq 1100\text{K}$. This is summarised in a cartoon in Fig. 13. The grains can grow by implantation of carbon ions they collide with in the wind and this process is greatly helped if the grains are forced to move through the wind by radiation pressure – which they certainly experience. Evidence for larger grains made in WR 140 comes from the eclipses observed in the optical light curves between phases 0.020 and 0.055 by Marchenko et al.

The *K* and *L'* light curves show an inflexion at $\phi = 0.14$, suggesting a short-lived increase in dust emission. The *H* photometry does not show any interruption in its fading at this phase, suggesting that the brightening at *K* and *L'* does not come from the condensation of new, hot dust but from a temporary increase in the growth rate of the grains.

After $\phi = 0.14$, the fading continues at all wavelengths and the dust cools as expected. The total mass, however, falls from its maximum of $6.5 \times 10^{-8} M_\odot$ to less than $3 \times 10^{-8} M_\odot$. It suggests that, as grains move through the wind, the rate of destruction by thermal sputtering eventually overtakes that of growth by implantation of carbon ions and grains are destroyed.

The light curves give invaluable information on the integrated properties of the dust, including its radial expansion, and are nicely complemented by imaging observations, which map the dust on the sky and allow us to relate it to the orbit. The dust emission by WR 140 was first imaged in 2001 (phases 0.04 and 0.06) by Monnier, Tuthill & Danchi (2002) with the Keck telescope. More images at wavelengths between 2.2 μ and 12.5 μm were observed in a multi-site campaign by Sergey Marchenko, Tony Marston, Tony Moffat, Watson Varricatt and the author using the Hale 5-m telescope, William Herschel Telescope (WHT), UKIRT and Gemini North with infrared cameras and, in some cases, adaptive optical systems. As the dust cooled, it was necessary to observe it at longer wavelengths. Details are given by Williams et al. (2009). The phases of the observations are marked on the light curves closest in wavelength to the images in Fig. 12 with ‘H’ (Hale), ‘W’ (WHT), ‘U or UIST’ (UKIRT) and ‘G’ (Gemini). A montage of images, all on the same scale, is presented in Fig. 14. We see dust features to the S and E of the stars (which are not resolved), expanding away from them. The features look like clumps but are better described as concentrations in extended emission with brightness enhanced by the maximum entropy reconstruction processing of the images. (The two compact features close to the stars in the 2004.7 image are instrumental artefacts.)

The positions of persistent features, ‘C’ at the west end of the ‘bar’ to the south of the stars, ‘C0’ at the east end of the ‘bar’ and ‘E’ in the feature to the east, have been measured. The position angles of each are constant, showing radial motion, and the distances are plotted against date and phase in Fig. 15. Within the errors, the proper motions are constant, suggesting that the dust is moving

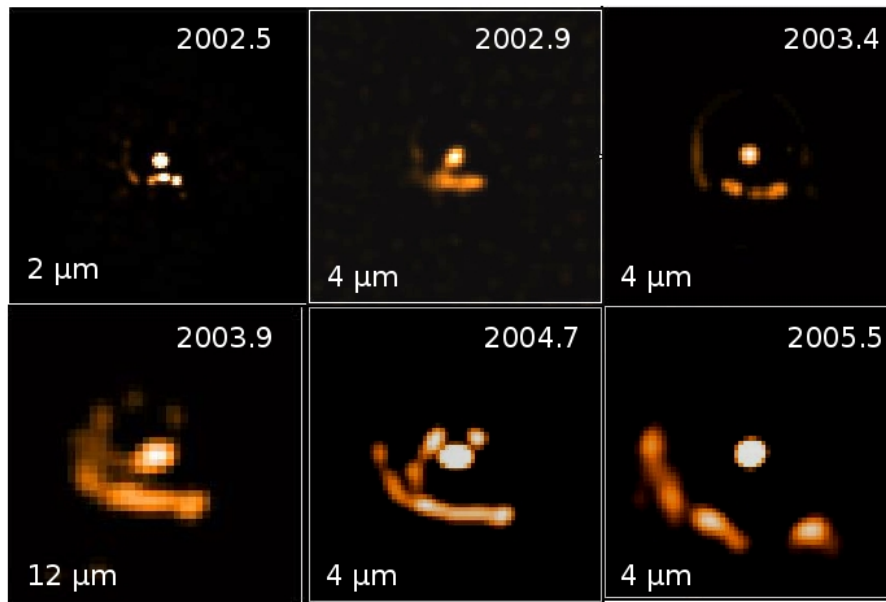


Figure 14: Infrared images of WR 140 all on the same scale, $4''$ square, with North at the top, East to the left, with dates and wavelengths of observations.

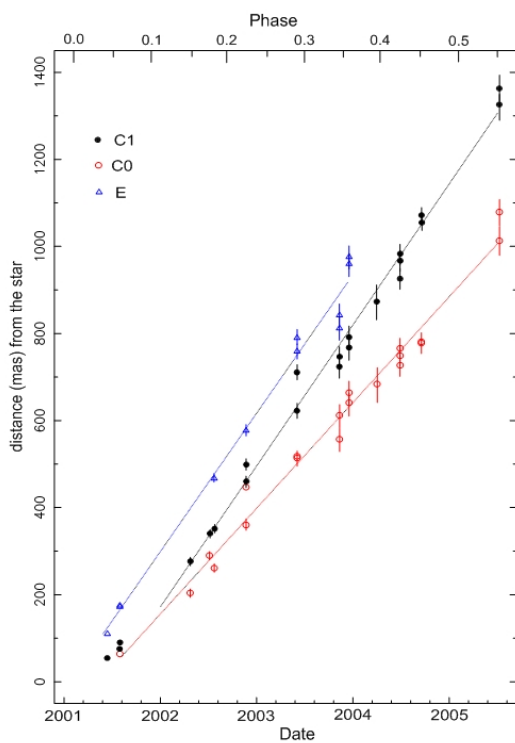


Figure 15: Radial distances (mas) of dust features (see text) against date and phase.

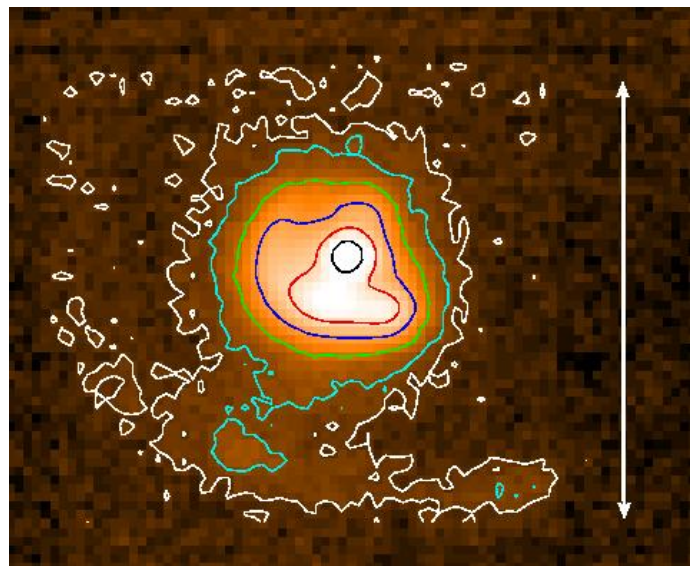


Figure 16: Combined 2003 November+December $12.5\text{-}\mu\text{m}$ image ($5''$ scale marker) at a more sensitive intensity scale than Fig. 14 to show the faint emission from the 1993 dust-formation episode to the south-east and south-west of the 2001 dust feature.

into a ‘clean’ environment, presumably cleared by the O5 and WC stellar winds. Some of the long-wavelength images (Fig. 16) show dust features corresponding to ‘C’ and ‘C0’ but further away – at distances which fit the extrapolated proper motions derived from the 2001 dust!

The constancy of the proper motions seems surprising given that the grains must experience radiation pressure: a 100\AA located 100 AU from the O5 and WC stars will gain 100 km s^{-1} in velocity within one week. But as a grain accelerates to move faster than the wind, it experiences supersonic drag, which increases with the square of the velocity relative to the wind until the radiation pressure is balanced by the drag and the grain has a constant, ‘drift’, velocity relative to the wind. The expansion velocity of the dust is then the sum of V_{flow} , inherited from the compressed wind, and the drift velocity. Projection of the proper motions back to the stars suggests that feature ‘E’ was formed about 136 d. (0.05 P) before ‘C’ and ‘C0’.

The images allow us to separate photometry of the dust features from that of the stars and, when we have images at two wavelengths (e.g. 3.6μ and $3.99\mu\text{m}$ on UKIRT or $7.9\mu\text{m}$ and $12.5\mu\text{m}$ on Gemini), we can determine infrared colours. The results show that the dust features are ‘redder’ than the stars in ([3.6]–[3.99]), as expected from heated dust and stellar wind emission, but ‘bluer’ in ([7.9]–[12.5]). The latter may be surprising but is correct: at the time of the observations, the dust emission peaked at a wavelength shorter than $7.9\mu\text{m}$, and the Rayleigh-Jeans tail of the Planckian dust spectrum is steeper than the spectrum of the free-free emission from the stellar wind.

Relation of the dust maps to the projected orbit is difficult. From combination of their radio images with the RV orbit, Dougherty et al. derived i and Ω , orienting the orbit on the sky. They noted that the O5 star was NW of the WC7 star at the time of periastron, and commented on the paucity of dust in that direction given that the base of the WCR (i.e. the open end), where dust was expected to form, would have been pointing in that direction. Owing to the high orbital eccentricity, however, the position angle of the WCR changes very rapidly around periastron passage (e.g. the P.A. of the O5 star relative to the WC star moves through three-quarters of its orbit in only 0.04P. These ranges are very sensitive to the orbital eccentricity itself, because it is so high, and account for the spreading of the dust around much of the orbit despite the short duration of dust formation. Also, the density along the dust plume varies sharply with P.A. Even if dust forms at a constant rate, the density on the sky of dust condensed from the compressed wind originating at periastron is more than ten times lower than that originating at phase 0.02, where the WCR sweeps round more slowly, and the dust is spread less thinly.

Models for the dust emission have been constructed using the orbit, timing of dust formation from the IR light curves, V_{flow} and the shape of WCR from the winds, populating the down-stream WCR with dust. This is projected on the sky to get images for comparison with the observed images. The model images are very sensitive to the orbital elements, especially eccentricity, and the fits are improved by dropping the assumption that the wind densities in the WCRs are uniform around their axes and having higher densities on the ‘trailing edge in the plane, which is consistent with some models of WCRs. This also accounts for the lower proper motion of one of the dust features (‘C0’, Fig. 15).

Successful modelling of the dust formation by WR 140 is the biggest test of the colliding-wind dust-formation paradigm because we know so much about this system; if we cannot model it, we cannot claim to understand dust formation by the CWBs. And, in any fitting process, we should remember the words of John von Neumann (as quoted by Enrico Fermi) “with four parameters I can fit an elephant and with five I can make him wiggle his trunk.”

Acknowledgements

The author is grateful to the Institute for Astronomy for hospitality and continued access to facilities of the Royal Observatory, Edinburgh.

References

- Cantó J., Raga A. C., Wilkin F. P., 1996, *ApJ*, 469, 729
Dougherty S. M., Beasley A. J., Claussen M. J., Zauderer A., Bolingbroke N. J., 2005, *ApJ* 623, 447
Lührs S., 1997, *PASP*, 109, 504
Marchenko S. V., et al., 2003, *ApJ*, 596, 1295
Monnier J. D., Tuthill P. G., Danchi W. C., 2002, *ApJ*, 567, L137
Pollock A. M. T., Corcoran M. F., Steven I. R., Williams P. M., 2005, *ApJ* 629, 482
Varricatt W. P., Williams P. M., Ashok N. M. 2004, *MNRAS*, 351, 1307
Williams P. M., Stewart J. M., Beattie D. H., Lee T. J., 1977, *IAU Circ.* 3107, 2
Williams P. M., Beattie D. H., Lee T. J., Stewart J. M., Antonopolou E., 1978, *MNRAS* 185, 467
Williams P. M., Marchenko S. V., Marston A. P., et al. 2009, *MNRAS* 395, 1749